Approach for simultaneous measurement of two-dimensional angular distribution of charged particles: Spherical aberration correction using an ellipsoidal mesh

H. Matsuda and H. Daimon

Graduate School of Materials Science, Nara Institute of Science and Technology (NAIST),
8916-5 Takayama, Ikoma, Nara 630-0192, Japan
and CREST, Japan Science and Technology Agency (JST), 4-1-8 Honcho, Kawaguchi, Saitama 332-0012, Japan

M. Kato and M. Kudo

JEOL Ltd., 1-2 Musashino 3-chome, Akishima, Tokyo 196-0021, Japan

An approach for simultaneous measurement of two-dimensional angular distribution of charged particles is proposed. This concerns spherical aberration correction in electrostatic lenses with potential use of a mesh. In an earlier work, an effective use of a spherical mesh has succeeded to obtain a large acceptance angle limited to around 60° (±30°). The present work is aimed at dramatically increasing acceptance angles limited in conventional lenses. For this purpose, spherical aberration behavior of mesh lenses is studied in detail using an analytical approximation and ray tracing, with particular attention paid to the effect of the mesh shape. It is shown here that the lens ability to correct spherical aberration over wide aperture angles can be effectively enhanced by the ellipsoidal deformation of a spherical mesh. We demonstrate that an effective use of an ellipsoidal mesh provides remarkable performance characteristics for electrostatic lenses, which opens new possibilities in surface and materials analysis techniques. Simple examples of ellipsoidal mesh lenses are presented that allow very wide acceptance angles of up to 120°.

I. INTRODUCTION

There are various ways to obtain atomic scale information by exploiting the energy and angular distribution of charged particles. Photoelectron angular distribution (PEAD) at relatively low kinetic energy contains valuable information on the electronic, structural, and dynamic characteristics of materials. [1–5]. Measurement of PEAD at high energies above several hundred eV, giving a photoelectron diffraction pattern, allows determination of atomic arrangement and adsorption geometry [6–8]. Photoelectron holography [9,10] has been developed to produce three-dimensional atomic images using photoelectron diffraction patterns. The novel method of "stereo atomscopy," which was proposed by Daimon [11], enables direct recognition of three-dimensional atomic structure by taking advantage of the phenomenon of circular dichroism in PEAD. The method is applicable to various materials including organic molecules and polymers.

To obtain detailed structural and electronic information using methods such as mentioned above, data collection over wide emission angles is required. For this measurement, two basically different approaches are present: a conventional approach, which is used in many electron spectroscopic techniques such as XPS (x-ray photoelectron spectroscopy), and an approach like the one used in the display-type spherical-mirror analyzer [12–14], which was used for three-dimensional band mapping [15] and to produce stereo atomic images [11,16]. In the conventional approach, emitted electrons are collected by some lens system and then focused onto the entrance of an energy analyzer, after which PEAD images can be produced. The lens system can provide some useful functions: an imaging function, selected-area observation using a field-limiting aperture, and improving energy resolution by decelerating electrons. However, angular acceptance of such an instrument is not large (around ±15° or less) and data collection over many different emission angles is not efficient. Moreover, it seems to be almost impossible to use the case for real time observation of PEAD, since measurements at different emission angles will be done with some time interval, with rotating a sample or an optical system. In contrast, the display-type spherical-mirror analyzer enables simultaneous angle-resolved measurement over very wide angular acceptance of ±60°. However, in this case, functions like those of the conventional approach are not given, with emitted electrons directly introduced into the analyzer. To overcome the disadvantages of the two approaches, we solve the problem of spherical aberration.

It is well known that in usual electron lenses (or to be precise, in rotationally symmetric, static electromagnetic fields with no space charge), spherical aberration cannot be avoided, with its sign always positive [17]. To overcome the spherical aberration in electron lenses, several correction methods have been developed. A typical method is that of using electrostatic or magnetic multipoles [18–21] (i.e., the use of nonrotational-symmetric optics): quadrupole-octopole corrector [18] and double-hexapole corrector [21]. In this method, third-order spherical aberration can be corrected with a precisely aligned optical assembly. As a result, using multipole correctors, significant improvement of spatial resolution was realized in transmission and scanning electron microscopes [22,23] (in which the beam angle divergence is set very small). However, for systems with large acceptance angles, higher-order spherical aberrations are no longer negligible and their correction becomes very important. Another straightforward attempt is to introduce space charge [24,25] instead of giving up rotational symmetry. The potential approach that is rather practical and equivalent to the space-charge method is the use of electron-transparent foils or

meshes in its combination with electrostatic or magnetic lenses [26,27]. A computational approach is the reconstruction method known as defocus-image modulation processing [28,29], which enables spherical aberration-free imaging under a conventional electron microscope by processing a through-focal-series of images.

After the pioneering work of Scherzer [26], the method of using foils or meshes has been extensively studied and applied in various fashions [30–40]. It allows us to deform electrostatic fields effectively, in such a way that *locally negative* spherical aberration is produced or enlarged. (The spherical aberration in any conventional electrostatic lens can be locally negative, while it always becomes positive after the total lens field.) The use of flat foils or meshes enables correcting third-order spherical aberration, but it is difficult to simultaneously correct higher-order spherical aberrations. In this context, the use of curved meshes was studied and significant improvements were found in the performance of mesh lenses [37–39]]. In particular, an effective use of a spherical mesh has been proposed by Kato and Sekine [39], showing that it is possible to correct spherical aberration over an aperture angle up to 60° (±30°). Here, it is important to note that the effect of a curved mesh can be greatly enhanced by the arrangement of electrodes around the mesh, while in earlier studies [30,37], no substantial improvements were found for equidiameter cylinder lenses by using a spherical foil instead of a flat foil.

Our aim is to enlarge dramatically the acceptance angles limited in conventional lenses. If this can be done, then extraordinary functional development, as well as a considerable improvement of sensitivity, can be accomplished in surface and materials analysis techniques such as XPS. Given an objective lens with an acceptance angle larger than 90° (±45°) at a kinetic energy of around 1 keV, a special atomscope can be constructed so that we obtain a stereo atomic image in a practical way. This instrument will enable combining microscopic and stereo atomic images by changing modes, hence it will allow viewing three-dimensional atomic structure in selected microscopic areas. In XPS analysis, acceptance angles larger than 90° will allow simultaneous measurement of all angular dependence of photoelectrons from glancing angle to surface normal, by which depth profile analysis based on angle-resolved spectroscopy becomes very efficient.

Motivated by the above, we study the possibility of the use of meshes for spherical aberration correction over very wide aperture angles. Starting with mesh lenses proposed in Ref. [39], we consider the ellipsoidal deformation of spherical meshes to enhance their correction abilities. A somewhat similar approach was proposed in Ref. [37], introducing meshes with the shape of a Bessel function. Our approach, in which a mesh is placed at the entrance of electrostatic lenses, attempts to give effective forces to electrons after passing through the mesh while keeping a sample region field-free. What is required here is that the mesh, together with some electrodes around it, locally generates a significant amount of negative spherical aberration to compensate positive spherical aberration accompanying a focusing field. In connection with whether this regime holds for wide acceptance angles, we study in detail the spherical aberration behavior around a

mesh focusing on the effect of the mesh shape. After this local analysis, our attention is directed to the whole design of ellipsoidal mesh lenses, which requires optimization of the mesh shape, the arrangement of electrodes, and the voltages on them. We show the correction ability of ellipsoidal mesh lenses for very wide acceptance angles up to 120°.

In the next section, we evaluate the mesh effect on virtual images by means of a first-order approximation and a ray tracing analysis. Here some important features involved in our approach are discussed. In Sec. III, a practical lens design with an ellipsoidal mesh is presented, demonstrating the effectiveness of our approach. In Sec. IV, detailed deformation of an exact ellipsoidal mesh is taken into account to further enhance the performance of mesh lenses. Here a mesh lens with an acceptance angle of 120° is exhibited. Section V is devoted to discussion and conclusion.

II. SPHERICAL ABERRATION BEHAVIOR IN THE FIELD AROUND A MESH

To enhance the correction ability of mesh lenses proposed in Ref. [39], we consider the deformation of spherical meshes to ellipsoidal shapes. Following the manner in Ref. [39], we estimate the spherical aberration generated by *the field around a mesh* in order to manifest the effect of the deformation. Here *the field around a mesh* is defined as its boundary being given by a certain equipotential surface that is highly affected by the mesh. Before showing results of a ray tracing analysis, we give an indication of a first-order approximation.

A. Basic analysis: A first-order approximation

Let us consider a mesh with a shape of a rotationally symmetric ellipsoid. We deal with a situation where the inside of the mesh is field-free and an electrostatic field is present in the outside of the mesh (or more specifically, the situation that the mesh and the sample are both grounded and an electrostatic field is generated between the mesh and electrodes around it). Let us choose the source of electrons at the origin O of the coordinate system and let the center O_e of the ellipsoid be at a distance d from O, as shown in Fig. 1. Then the electron trajectory started at O with an angle θ crosses the mesh S_0 at a distance $\rho(\theta)$ of the form

$$\rho(\theta) = \frac{d + \sqrt{a^2(1 + \gamma^2 \tan^2 \theta) - \gamma^2 d^2 \tan^2 \theta}}{\cos \theta (1 + \gamma^2 \tan^2 \theta)}, \quad (2.1)$$

where $\gamma = a/b$ is the ratio of the two radii a and b of the ellipsoid (with a in the optical axis z and b along its vertical axis x).

We can simply evaluate spherical aberration behavior around the mesh by means of a first-order approximation. We focus on virtual images from a certain equipotential surface S_1, at which electron trajectories are terminated. Here we define the axially crossing position z_c in the virtual image space by

$$z_c = z_1 - x_1/\tan \theta_1, \quad (2.2)$$

where (z_1, x_1) is the point of a trajectory on S_1 and θ_1 is the angle between the z axis and the velocity vector at (z_1, x_1).
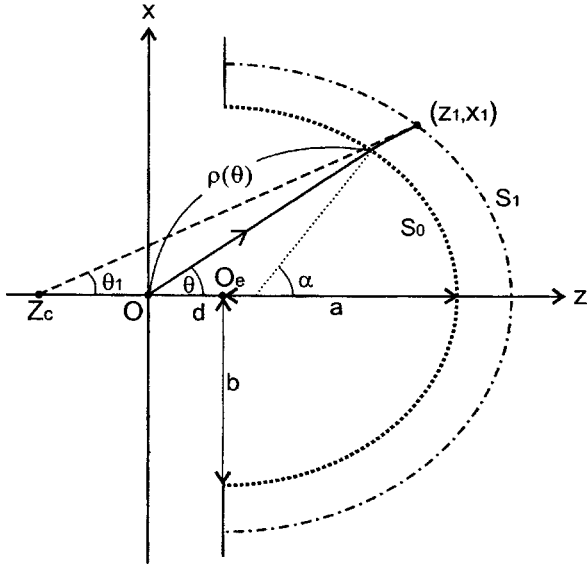
FIG. 1. Illustration of the use of an ellipsoidal mesh. The mesh surface is indicated by the dotted line. The rotational symmetry axis of the mesh coincides with the optical axis z. The inside of the mesh is field-free and the outside is given a certain electrostatic field. A trajectory, started at the coordinate origin O, is terminated at a certain equipotential surface S_1, at which a virtual image is considered.

Consider a narrow region between two equipotential surfaces S_0 and S_1, and assume that in this region, an electron is subjected to an electrostatic field perpendicular to the mesh surface. The angle α between the z axis and the line of the force direction at (z_1, x_1) is given by $\tan \alpha = \gamma^2 \rho(\theta) \sin \theta / [\rho(\theta) \cos \theta - d]$. Then, performing the first-order approximation in the region, we obtain the axially crossing position in the virtual image space as follows:

$$\frac{z_c(\theta)}{b} = \frac{K}{2}\left(\gamma + \frac{d/b}{F}\right)\frac{(1-\gamma^2)F - \gamma(d/b)(1+\tan^2\theta)}{\cos^2\theta(1+\gamma^2\tan^2\theta)^2},$$
(2.3)

with

$$F = \sqrt{1 + \gamma^2\tan^2\theta - (d/b)^2\tan^2\theta}$$
(2.4)

and $K = -e\Delta\phi/E_0$, where $\Delta\phi = \phi_1 - \phi_0$ is the potential gap between S_0 and S_1, and E_0 is the initial energy of an electron. Here and in subsequent sections, some quantities of interest are scaled by b. For the simplest case of $\gamma = 1$ and $d = 0$, no spherical aberration occurs naturally [$z_c(\theta) = 0$, irrespective of θ].

Let us look at Eq. (2.3) for two simple cases: (a) $\gamma = 1$ (the spherical mesh case) and (b) $d = 0$ (the electron source at the center of the ellipsoid). Then Eq. (2.3) results in

$$\left.\frac{z_c(\theta)}{b}\right|_{\gamma=1} = -\frac{K}{2}\frac{d}{b}\left(1 + \frac{d/b}{\sqrt{1+(1-d^2/b^2)\tan^2\theta}}\right)$$
(2.5)

and

$$\left.\frac{z_c(\theta)}{b}\right|_{d=0} = \frac{K}{2}\frac{\gamma(1-\gamma^2)}{\cos^2\theta + \gamma^2\sin^2\theta}\frac{1}{\sqrt{1+\gamma^2\tan^2\theta}}.$$
(2.6)

The sign of the spherical aberration changes depending on K, γ, and d. In the virtual-image discussion, negative spherical aberration means that trajectories with larger initial angles cross the optical axis at larger z. We are concerned with the case of $K > 0$, which means that there is a deceleration field. [The spherical aberration behavior of the case $K < 0$ is opposite to that of the case $K > 0$, according to Eq. (2.3).] It is easy to see that in the case $\gamma = 1$ ($K > 0$), negative spherical aberration occurs for $d/b < 1$, while the region $d/b > 1$ yields positive spherical aberration. Here $d/b = 1$ gives the boundary condition with no spherical aberration [$z_c(\theta)/b = -K$, irrespective of θ]. In the case $d = 0$, negative spherical aberration occurs for $\gamma > 1$, the case where the longer radius is in the optical axis. In Fig. 2, characteristic behaviors of spherical aberration are exhibited by plotting Eqs. (2.5) and (2.6) as functions of θ for some variations of d and γ [Eq. (2.5) corresponding to Fig. 2(a) and Eq. (2.6) to Fig. 2(b)]. Here initial angles θ up to $\theta_{max} = \arctan(b/d)$ are considered. For this upper limit, Eq. (2.3) gives $z_c(\theta_{max})/b = -(K/2)[(d/b)^3 + d/b]$. It is indicated in Fig. 2(b) that negative spherical aberration can be enlarged by increasing the ratio γ. In the general case of Eq. (2.3), similar behavior of spherical aberration is found when increasing γ. An example is presented in Fig. 2(c), in which the γ dependence of spherical aberration behavior is shown for $d/b = 0.5$. Note that in this case the amount of negative spherical aberration is enlarged, compared with that in Fig. 2(b).

The enlargement of negative spherical aberration in the above manner will be the key to the spherical aberration correction over very wide aperture angles. This is discussed in detail in the following.

B. Ray tracing analysis

We present here a ray tracing analysis of the spherical aberration generated by the field around a mesh. The charge simulation method was used to calculate electrostatic fields. We first consider a spherical mesh lens that allows an acceptance angle of 60°. Figure 3 shows the electron trajectories in this lens that are started in two different situations and terminated at a certain equipotential surface. Here virtual images are considered in the same manner as in Sec. II A. The position of the lens entrance in Fig. 3(a) is just the case where an acceptance angle of 60° is allowed, and that in Fig. 3(b) is a case of access to larger entrance angles. In Fig. 3(a), it is important to note that large negative spherical aberration is generated to compensate large positive spherical aberration accompanying a focusing field.

In Fig. 4, we show axially crossing positions $z_c(\theta)$ as functions of initial angles, for some variations of the distance d. The lowest curve ($d/b = 1.44$) is the case corresponding to Fig. 3(a). It is indicated that the amount of negative spherical aberration considerably decreases with a decrease of the distance d. Note that the spherical aberration behavior in Fig. 4 is different from that in Fig. 2(a), in which the amount of negative spherical aberration is much smaller. Thus large
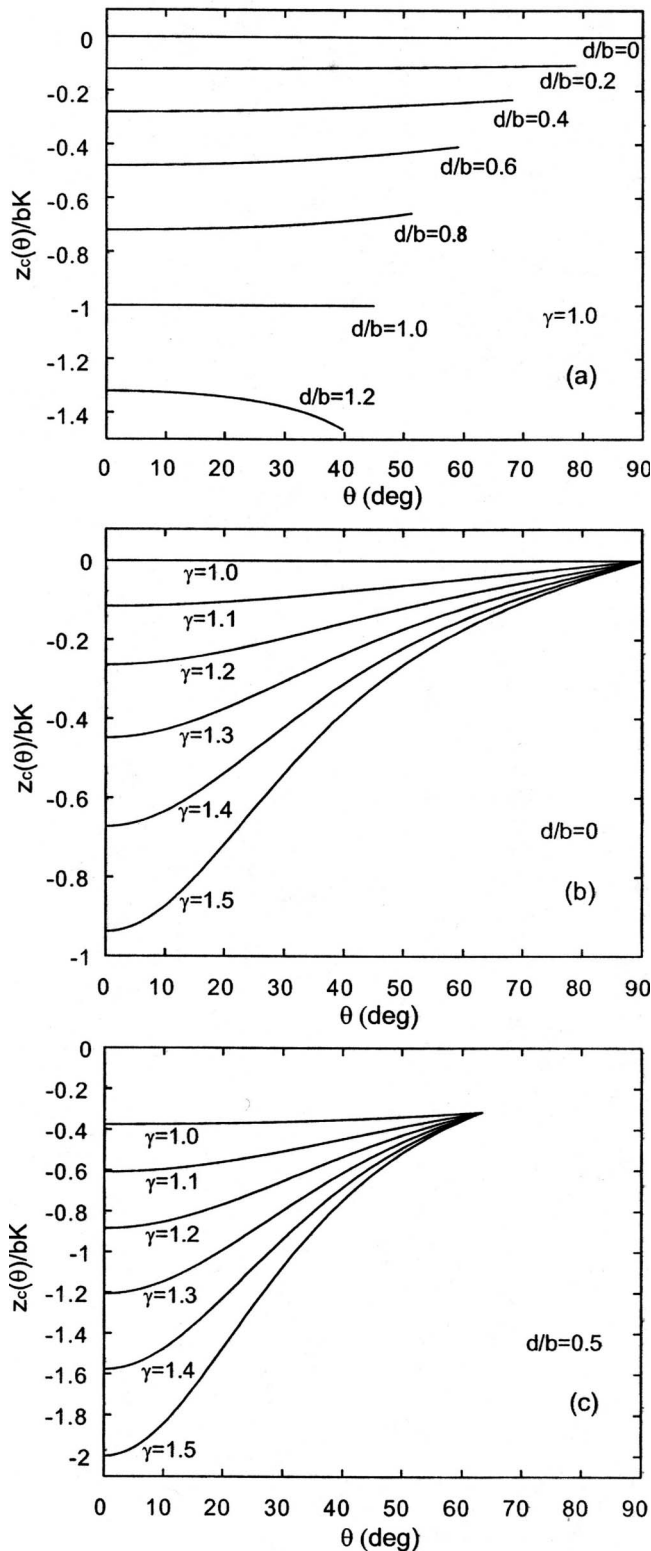
FIG. 2. Some aspects of spherical aberration behavior estimated by a first-order approximation. The axially crossing positions z_c in the virtual image space as functions of initial angles θ are plotted showing (a) the dependence of spherical aberration behavior on the distance d for the spherical mesh case $\gamma=1$, and (b),(c) the dependence of spherical aberration behavior on the ellipsoid parameter γ for $d=0$ and $d/b=0.5$.
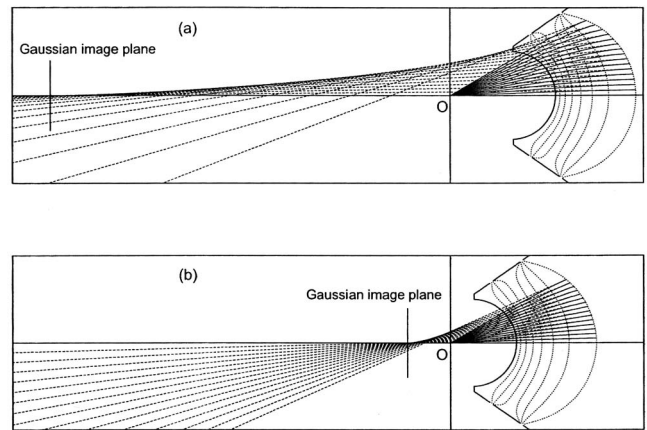

FIG. 3. Partial electron trajectories with initial angles up to $\pm 30°$ calculated in a spherical mesh lens. Two situations are considered in the choice of the distance d: (a) $d/b=1.44$ and (b) $d/b=0.54$. The trajectories, after passing through the field-free region, are affected by a certain deceleration field and terminated at a certain equipotential surface. The dotted lines indicate equipotential surfaces of the field around the mesh. Spherical aberration behavior in the virtual image space is seen by the dashed lines.

negative spherical aberration in Fig. 4, required for an acceptance angle of 60°, is generated by deforming a spherically distributed field by means of electrode conditions. However, unfortunately for small d, negative spherical aberration cannot be effectively enlarged by means of electrode conditions in order to cancel large positive spherical aberration of the subsequent field. This leads to the limitation in acceptance angles at around 60° when using spherical meshes.

To overcome this limitation, we now consider the use of an ellipsoidal mesh in its combination with electrodes designed for a large entrance angle. We show in Fig. 5 the partial electron trajectories calculated under a certain elec-
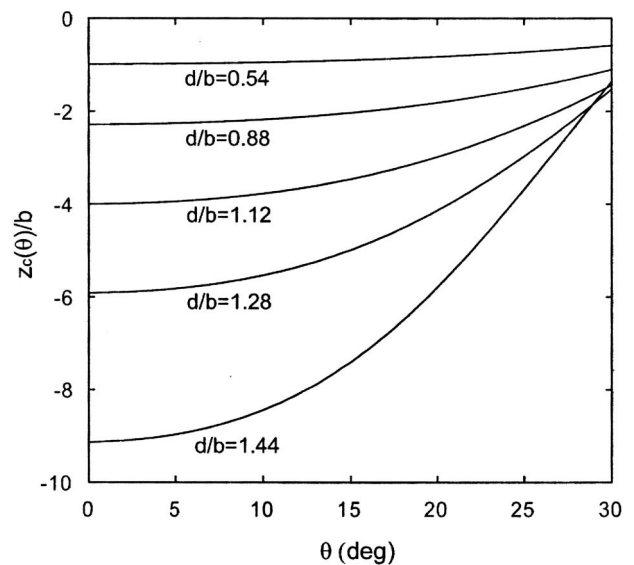

FIG. 4. Ray tracing results for the axially crossing positions z_c in the spherical mesh case. The dependence of spherical aberration behavior on the distance d is shown.
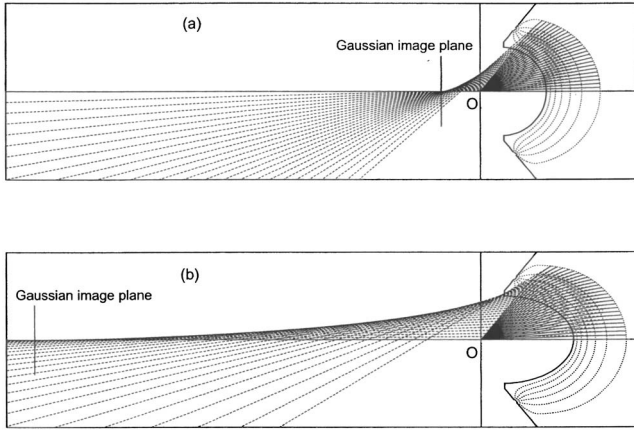
FIG. 5. A manifestation of the effect of the mesh shape in comparison between (a) a spherical mesh lens ($\gamma=1$) and (b) an ellipsoidal mesh lens ($\gamma=1.6$). The latter lens is given by the ellipsoidal deformation of the spherical mesh in the former lens, with other conditions fixed. Trajectories with initial angles up to $\pm50°$ are shown.

trode condition, for two cases of mesh shape: $\gamma=1.0$ (a spherical mesh case) and $\gamma=1.6$ (an ellipsoidal mesh with longer radius in the optical axis). Here initial angles up to $50°$ are considered. Figure 5(b) demonstrates that an ellipsoidal mesh with $\gamma>1$, together with some electrodes around it, actually yields large negative spherical aberration. The axially crossing positions z_c in the virtual image space as functions of initial angles are shown in Fig. 6 for some variations of the ratio γ. Again, it is seen that negative spherical aberration can be effectively enlarged by increasing the ratio γ. In Fig. 6, we emphasize that the effect of the change in γ is greater for trajectories with smaller initial angles, while lens fields in general have a greater effect on trajectories with larger initial angles. As a result, spherical aberration correc-
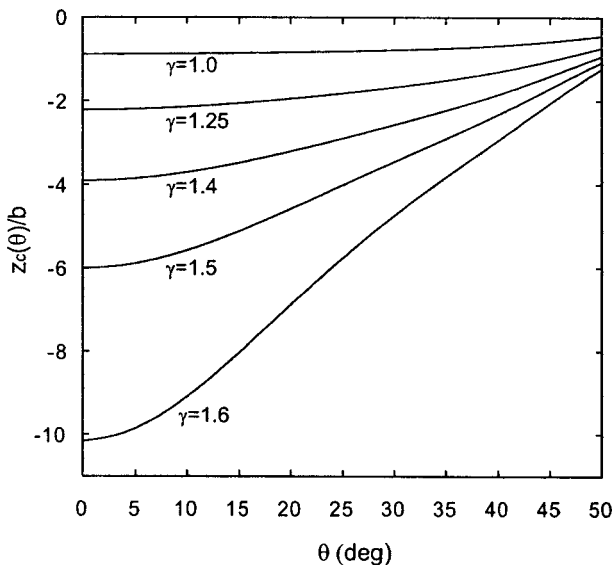

FIG. 6. Ray tracing results for the axially crossing positions z_c in the ellipsoidal mesh case. The dependence of spherical aberration behavior on the ellipsoid parameter γ is shown.
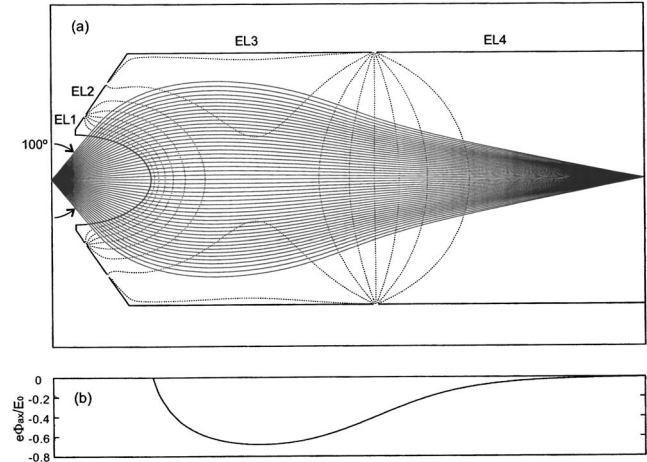

FIG. 7. A four-electrode lens with an ellipsoidal mesh. Trajectories with initial angles up to $\pm50°$ are considered and successful cancellation of locally generated negative and positive spherical aberrations is realized. The equipotential surfaces are indicated by the dotted lines. The lower figure shows the axial potential distribution of the system above.

tion over very wide aperture angles becomes possible with an effective use of ellipsoidal meshes.

III. SPHERICAL ABERRATION CORRECTION USING AN ELLIPSOIDAL MESH

As shown in the previous section, negative spherical aberration generated by the field around a mesh can be effectively controlled by the ellipsoidal deformation of the mesh. We now proceed to the use of this feature for the cancellation of positive spherical aberration accompanying a focusing field, i.e., the correction of spherical aberration in the whole lens field. To do this, it is required to optimize several parameters including electrode conditions and shape parameters of the mesh.

A number of solutions are possible in the design of ellipsoidal mesh lenses. As a simple example, a four-electrode lens with an ellipsoidal mesh is shown in Fig. 7(a). Here the first electrode EL1, the mesh, and the final electrode EL4 are set at ground potential. Negative voltages are applied to the intermediate electrodes EL2 and EL3; thus the whole lens field is a combination of deceleration and acceleration fields, similar to an einzel-type lens. Electron trajectories with initial angles up to $\pm50°$ and equipotential lines are shown in the figure. Figure 7(b) displays the axial potential distribution Φ_{ax} relative to E_0/e (E_0 is the initial energy of an electron and e is the elementary charge). The ratio γ of the two radii of the considered ellipsoid is $\gamma=1.73$. We emphasize that a very large acceptance angle of $100°$ can be attained in a simple lens design by using an ellipsoidal mesh.

The correction ability of the mesh lens largely depends on the ratio γ. To show this, we have performed the optimization of electrode conditions for various values of γ, starting from the spherical mesh case $\gamma=1$. In Fig. 8, we plot the results for the spherical aberration disk size (the size of blurring of electron trajectories at the image plane that is caused
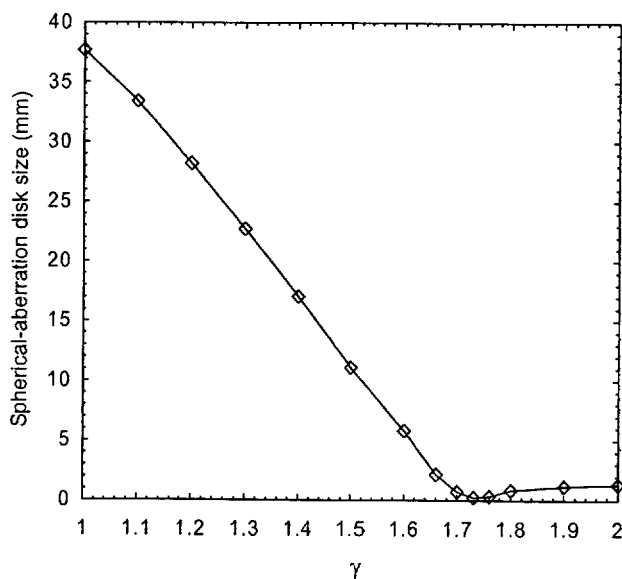
FIG. 8. Estimation of the aberration disk size in ellipsoidal mesh lenses with an aperture angle of 100°. Various values of the ellipsoid parameter γ including the spherical mesh case are considered. Shown are the results obtained by the optimization of electrode conditions. The distance between the object and the image is set to 500 mm.
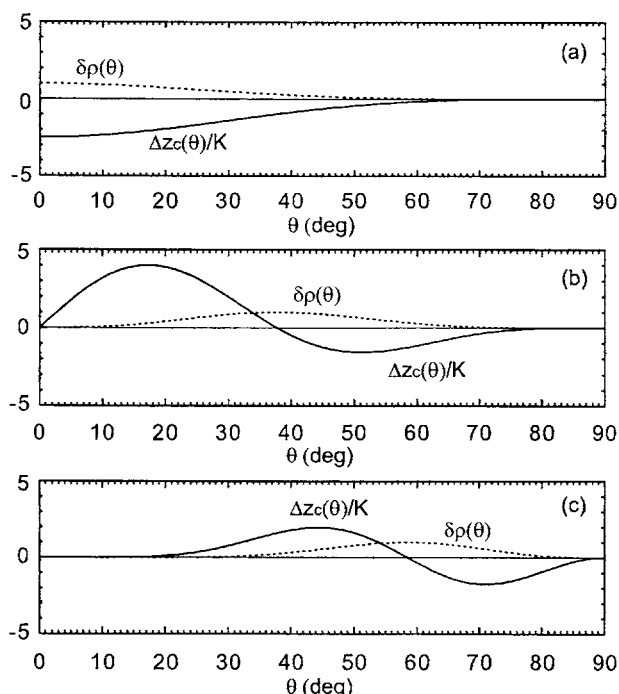

FIG. 9. Some examples of the deformation function $\delta\rho(\theta)$ in the form of Eq. (4.3) and evaluation of its contribution $\Delta z_c(\theta)$ to the axially crossing position in the virtual image space. $\Delta z_c(\theta)/K$ and $\delta\rho(\theta)$ are drawn by solid and dotted lines, respectively. Different choices of the parameters p and q are considered: (a) $p=0, q=5$, (b) $p=3, q=5$, and (c) $p=8, q=3$. The parameter c is set such that the maximum value of $\delta\rho(\theta)$ is unity.

by spherical aberration). Shown here are the values for the case where the distance between the object and the image is 500 mm; these values can be reduced in proportion to the system size. The correction ability dramatically increases from the spherical mesh case with increasing γ. There is a certain optimal value of γ around 1.73, above which a gradual increase of the aberration disk size is found.

IV. FINE CORRECTION OF SPHERICAL ABERRATION

While the considered mesh lens indeed allows very wide acceptance angles, some amount of spherical aberration always remains, meaning that exact ellipsoidal meshes are not completely optimal. It is thus reasonable to consider here detailed deformation of an exact ellipsoidal mesh in order to give a better correction ability for the mesh lens. To obtain some insight into this deformation, we again direct our attention to the discussion of virtual images in Sec. II A. Now, instead of Eq. (2.1), we describe the distance between the origin O and a mesh by

$$\rho'(\theta) = \rho(\theta) + \delta\rho(\theta). \tag{4.1}$$

This function should have a simple smooth surface topography that is close to the original function $\rho(\theta)$ (an exact ellipsoid), so that we suppose $\delta\rho(\theta)$ and $\partial\delta\rho(\theta)/\partial\theta$ to be very small. Then, we perform a first-order expansion of the perturbed axially crossing position $z_c'(\theta)$ which corresponds with Eq. (2.3) when $\delta\rho(\theta)=0$. According to this calculation, the change in the axially crossing position due to the deformation function $\delta\rho(\theta)$ is simply

$$\Delta z_c(\theta) = \frac{K}{2} \frac{1}{\sin\theta} \frac{\partial\delta\rho(\theta)}{\partial\theta}. \tag{4.2}$$

As shown in the preceding sections, the ellipsoid parameter γ allows us to increase or decrease negative spherical aberration of the field around a mesh and to find an optimal condition for compensating positive spherical aberration of a focusing field. However, this condition does not give complete cancellation of spherical aberration; it results in a non-monotonic dependence of spherical aberration on initial angles. Therefore, the detailed deformation is required to locally increase or decrease negative spherical aberration around a mesh. Equation (4.2) suggests that an effective local control can be made by introducing a smooth maximum or minimum in the function $\delta\rho(\theta)$.

As an example, we consider the function of the form

$$\delta\rho(\theta) = c \sin^{(p)}\theta \cos^{(q)}\theta, \tag{4.3}$$

where c, p, and q are adjustable parameters. This function has a maximum or minimum at $\theta_0 = \arctan(\sqrt{p/q})$. Inserting Eq. (4.3) into Eq. (4.2) gives

$$\Delta z_c(\theta) = c(K/2)(p \sin^{(p-2)}\theta \cos^{(q+1)}\theta - q \sin^{(p)}\theta \cos^{(q-1)}\theta). \tag{4.4}$$

This, together with Eq. (4.3), is plotted in Fig. 9 for some choices of p and q. Above and below θ_0, $\Delta z_c(\theta)$ has opposite contributions to the axially crossing position [as is clear from Eq. (4.2)], and consequently, the spherical aberration can be effectively regulated by properly choosing c, p, and q. Hence, it is useful to define the deformation function by

$$\delta\rho(\theta) = \sum_{i=1}^{n} c_i \sin^{(p_i)}\theta \cos^{(q_i)}\theta, \qquad (4.5)$$

with $3n$ adjustable parameters c_i, p_i, and q_i.

We have performed detailed deformation of the mesh shape using Eq. (4.5), through the ray tracing calculation and minimization of the spherical aberration disk size. Figure 10 shows an optimization result in the case of $n=4$. It is demonstrated in Fig. 10(a) that elimination of spherical aberration over a very wide aperture angle of 120° is possible. Figure 10(b) depicts the deformation function used in Fig. 10(a). As seen here, an optimal mesh shape can be obtained by a slight deformation of an exact ellipsoid. For different aperture angles, results of the detailed optimization for the spherical aberration disk size in the case of $n=4$ are given in Fig. 11. Here the results, compared with the exact-ellipsoidal mesh cases, show considerable improvement of the correction ability due to the detailed optimization. Further elimination of the spherical aberration is possible by performing optimization using more parameters.

V. DISCUSSION AND CONCLUSION

Spherical aberration correction in electrostatic lenses using ellipsoidal meshes has been proposed. The considered mesh lens consists of two opposite fields: the field around a mesh and a focusing field. For obtaining large acceptance angles, the former is required to locally generate large negative spherical aberration to compensate large positive spherical aberration caused by the latter. Some fundamental features of the mesh lens were highlighted in this regard, focusing on the mesh effect on virtual images. An important feature is that spherical aberration behavior around a mesh is greatly affected by the position of the electron source relative to the mesh; this feature involves even reversing the sign of the aberration. For small acceptance angles, there is a large degree of freedom to choose that position, which (as well as electrode conditions) can serve as an effective parameter to regulate negative spherical aberration. However, for wide or very wide acceptance angles, the object-mesh distance is severely restricted by the geometry of the space. We can then no longer correct spherical aberration using a spherical mesh even for smaller aperture angles, because of a considerable decrease in negative spherical aberration around the mesh. It was shown, however, that the negative spherical aberration can be effectively enlarged by the ellipsoidal deformation of a spherical mesh. This opens the possibility of the spherical aberration correction over very wide aperture angles.

As a simple application of our approach, we have designed a four-electrode lens with an ellipsoidal mesh. We then demonstrated that spherical aberration correction over very wide aperture angles is indeed possible. The spherical aberration dramatically decreases from the spherical mesh case as the major radius of the ellipsoid (which lies in the optical axis) increases relative to the minor radius. An optimal value for the ratio γ of the two radii is around $\gamma = 1.73$, for an aperture angle of 100°. Notice that this value has some sensitivity to the change in other conditions including the object position and electrode arrangement. The aberration
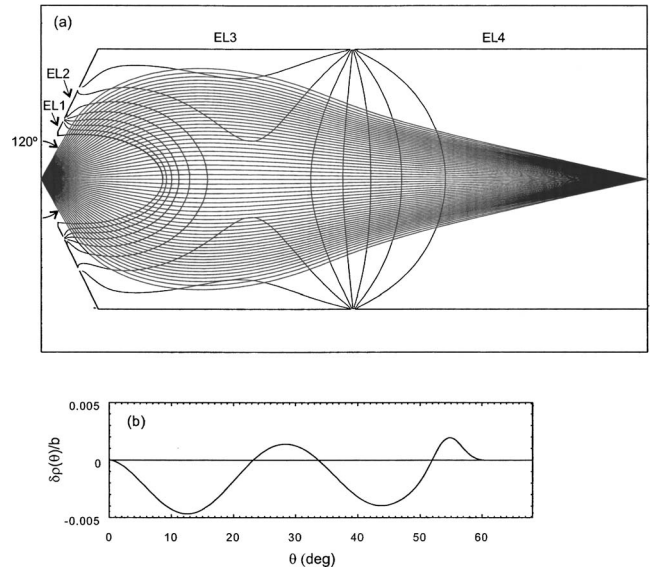

FIG. 10. Further enhancement of the mesh lens ability by means of detailed deformation of an exact ellipsoidal mesh: (a) A mesh lens with an enhanced correction ability. Trajectories with initial angles up to ±60° are shown. (b) The function $\delta\rho(\theta)$ used in the deformation. The relative value $\delta\rho(\theta)/b$ is very small, and thus the deformed mesh, shown in the upper figure, is close to the original (exact) ellipsoidal mesh.

disk size for the optimal γ is reasonably small and the simple ellipsoidal mesh lens can be used as an objective lens of, e.g., a simultaneous angle-resolved XPS spectrometer.

However, realization of high spatial resolution requires some improvement or modification of the lens design. The aberration disk size is greatly affected by electrons with larger initial angles and thus a simple solution is to design a mesh lens with some smaller acceptance angle. This possi-
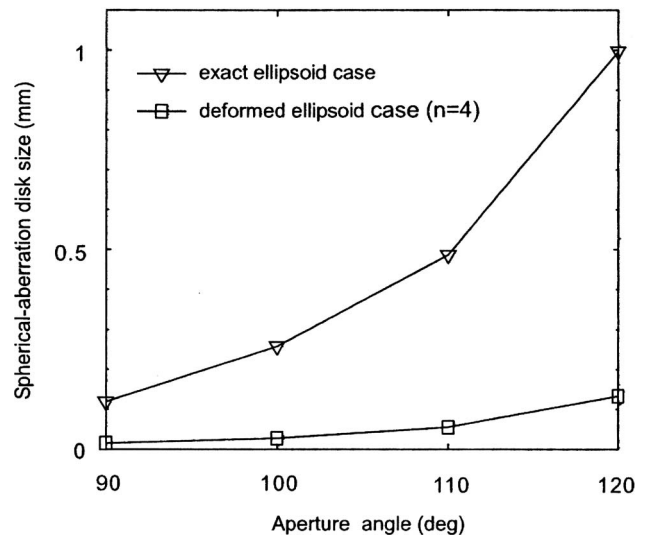

FIG. 11. Estimation of the spherical aberration disk size for mesh lenses with different aperture angles. The upper curve is the result for the exact ellipsoidal mesh case. The lower curve is the result for the deformed mesh case ($n=4$). The distance between the object and the image is set to 500 mm.

bility is of practical importance but at some disadvantage in our purpose. Another possibility is to use more electrodes around a mesh to control the electrostatic field more effectively. This may give a somewhat better correction without limiting the acceptance angle, but there will remain a certain amount of spherical aberration as long as we use an exact ellipsoidal mesh. From this viewpoint, we have formulated a detailed deformation treatment of the mesh shape. We have shown that in this manner it is possible to eliminate spherical aberration over a very wide aperture angle of 120°. However, note that the degree of the deformation is very small ($<0.5\%$), i.e., the original ellipsoidal mesh is close to the optimal one. This means that the approach, which allows delicate control of the electrostatic field, must be ensured by high-accurate mesh construction. For actual realization of high performance characteristics, it would, therefore, be practically better to take into account a moderate combination of the above possible treatments.

The remarkable consequence of this work provides a powerful means of simultaneous angle-resolved measurement of two-dimensional angular distribution of charged particles. Here, various analyses including photoelectron diffraction, photoelectron holography, stereo atomscopy, and depth profile analysis are expected to achieve very high efficiency, directly from the very wide acceptance angles. Note that in the proposed mesh lenses, a sample is placed in a field-free region, in contrast with the case of a cathode lens in a photoelectron emission microscope; accordingly, there is no serious restriction on sample treatment. As a result, by properly setting a sample, it is possible to perform simultaneous measurement of the angular dependence of electrons from perpendicular to parallel to a sample surface. Our particular interest is in the realization of the special atomscope mentioned in the Introduction; we emphasize that this is now possible. Our approach would serve as a basis for very fruitful development in surface and materials analysis techniques.

ACKNOWLEDGMENT

[1] T. Liebsch, O. Plotzke, F. Heiser, U. Hergenhahn, O. Hemmers, R. Wehlitz, J. Viefhaus, B. Langer, S. B. Whitfield, and U. Becker, Phys. Rev. A **52**, 457 (1995).

[2] E. Kukk, A. Wills, N. Berrah, B. Langer, J. D. Bozek, O. Nayadin, M. Alsherhi, A. Farhat, and D. Cubaynes, Phys. Rev. A **57**, R1485 (1998).

[3] R. Wiehle, B. Witzel, H. Helm, and E. Cormier, Phys. Rev. A **67**, 063405 (2003).

[4] T. Lischke, N. Bowering, B. Schmidtke, N. Muller, T. Khalil, and U. Heinzmann, Phys. Rev. A **70**, 022507 (2004).

[5] G. Turri, G. Snell, B. Langer, M. Martins, E. Kukk, S. E. Canton, R. C. Bilodeau, N. Cherepkov, J. D. Bozek, A. L. Kilcoyne, and N. Berrah, Phys. Rev. A **70**, 022515 (2004).

[6] A. Locatelli, B. Brena, G. Comelli, S. Lizzit, G. Paolucci, and R. Rosei, Phys. Rev. B **54**, 2839 (1996).

[7] F. Bondino, G. Comelli, A. Baraldi, R. Rosei, S. Lizzit, A. Goldoni, R. Larciprete, and G. Paolucci, Phys. Rev. B **66**, 075402 (2002).

[8] R. Terborg, M. Polcik, J. T. Hoeft, M. Kittel, D. I. Sayago, R. L. Toomes, and D. P. Woodruff, Phys. Rev. B **66**, 085333 (2002).

[9] D. Gabor, Nature (London) **161**, 777 (1948).

[10] J. J. Barton, Phys. Rev. Lett. **61**, 1356 (1988).

[11] H. Daimon, Phys. Rev. Lett. **86**, 2034 (2001).

[12] H. Daimon, Rev. Sci. Instrum. **59**, 545 (1988).

[13] H. Daimon and S. Ino, Rev. Sci. Instrum. **61**, 57 (1990).

[14] H. Nishimoto, H. Daimon, S. Suga, Y. Tezuka, S. Ino, I. Kato, F. Zenitani, and H. Soezima, Rev. Sci. Instrum. **64**, 2857 (1993).

[15] F. Matsui, Y. Hori, H. Miyata, N. Suganuma, H. Daimon, H. Totsuka, K. Ogawa, T. Furukubo, and H. Namba, Appl. Phys. Lett. **81**, 2556 (2002).

[16] F. Matsui, H. Daimon, F. Z. Guo, and T. Matsushita, Appl.

[17] O. Scherzer, Z. Phys. **101**, 593 (1936).

[18] H. Rose, Optik (Stuttgart) **33**, 1 (1971).

[19] A. V. Crewe and N. W. Parker, Optik (Stuttgart) **46**, 183 (1976).

[20] A. V. Crewe and D. Kopf, Optik (Stuttgart) **55**, 1 (1980).

[21] H. Rose, Optik (Stuttgart) **85**, 19 (1990).

[22] M. Haider, H. Rose, S. Uhlemann, E. Schwan, B. Kabius, and K. Urban, Nature (London) **392**, 768 (1998).

[23] J. Zach and M. Haider, Optik (Stuttgart) **98**, 112 (1995).

[24] E. A. Ash, J. Appl. Phys. **26**, 327 (1955).

[25] L. C. Chao, J. Orloff, and L. Wang, J. Vac. Sci. Technol. B **15**, 2732 (1997).

[26] O. Scherzer, Optik (Stuttgart) **2**, 114 (1947).

[27] O. Scherzer, J. Appl. Phys. **20**, 20 (1949).

[28] T. Ikuta, Appl. Opt. **24**, 2907 (1985).

[29] Y. Takai, T. Kawasaki, Y. Kimura, T. Ikuta, and R. Shimizu, Phys. Rev. Lett. **87**, 106105 (2001).

[30] J. L. Verster, Philips Res. Rep. **18**, 465 (1963).

[31] S. Maruse, S. Hiratake, and M. Ichihashi, Jpn. J. Appl. Phys. **9**, 1549 (1970).

[32] D. Typke, Optik (Stuttgart) **34**, 573 (1972).

[33] D. Typke, Optik (Stuttgart) **36**, 124 (1972).

[34] N. D. Wittels, J. Vac. Sci. Technol. **12**, 1165 (1975).

[35] E. Munro and N. D. Wittels, Optik (Stuttgart) **47**, 25 (1977).

[36] T. Hanai, M. Hibino, and S. Maruse, J. Electron Microsc. **33**, 329 (1984).

[37] A. A. van Gorkum, J. Vac. Sci. Technol. B **1**, 1312 (1983).

[38] A. A. van Gorkum and L. C. M. Beirens, J. Vac. Sci. Technol. A **4**, 2297 (1986).

[39] M. Kato and T. Sekine, J. Vac. Sci. Technol. A **13**, 2255 (1995).

[40] M. Kato and T. Sekine, J. Vac. Sci. Technol. A **14**, 453 (1996).

Phys. Lett. **85**, 3737 (2004).